Acetate electrosynthesis enables a low-carbon footprint chemical product chain

Authors: Roham Dorakhan[1,5], Ivan Grigioni[1,2,5], Byoung-Hoon Lee[1,5], Pengfei Ou[1], Jehad Abed[1], Colin O'Brien[3], Armin Sedighian Rasouli[1], Milivoj Plodinec[4], Rui Kai Miao[3], Erfan Shirzadi[1], Joshua Wicks[1], Sungjin Park[1], Geonhui Lee[1], Jinqiang Zhang[1], David Sinton[3], and Edward H. Sargent[1]*

Affiliations:

[1]Department of Electrical and Computer Engineering, University of Toronto, Toronto, Ontario, Canada.

[2]Dipartimento di Chimica, Università degli Studi di Milano, Via Golgi 19, 20133 Milano, Italy.

[3]Department of Mechanical and Industrial Engineering, University of Toronto, Toronto, Ontario, Canada.

[4]ScopeM, ETH-Zürich, Zürich, Switzerland

[5]These authors contributed equally: Roham Dorakhan, Ivan Grigioni, Byoung-Hoon Lee

*Corresponding author. Email: ted.sargent@utoronto.ca (E.H.S)

Abstract

The electrocatalytic synthesis of acetic acid from CO_2 offers a low carbon alternative for the production of an important chemical feedstock and precursor to polymers, solvents, food additives and textiles. CO electroreduction bypasses the CO_2 crossover energy penalty suffered by direct CO_2 electroreduction, motivating interest in a cascade approach of CO_2-to-CO followed by CO-to-acetic acid. However, for the process to achieve feasibility, major advancements in CO-to-acetate faradaic efficiency, partial current density, and product concentration are needed. Here we report a catalyst design strategy in which off-target intermediates are destabilized, an approach that leads to 70% faradaic efficiency (FE) to acetate at 200 mA cm^{-2} using an Ag-Cu_2O catalyst. We demonstrate 18 hours of stable operation in a membrane electrode assembly, with the system producing 5 wt.% acetate at 100 mA cm^{-2} and a full cell energy efficiency of 25%, a 2-fold improvement upon the highest-energy-efficiency electrosynthesis in prior reports.

Introduction

Electrification of chemical and fuel production offers a way to reduce carbon footprint and contribute to a circular carbon economy[1–3]. The electrocatalytic reduction reaction of CO_2 (CO_2RR) in electrolyzer cells enables the production of valuable liquid hydrocarbons such as ethanol, acetic acid, and propanol. With a market size of 13 billion USD and greenhouse gas (GHG) emissions averaging 1.8 kg CO_2-eq/kg, acetic acid is a feedstock for the synthesis of polymers, textiles and solvents and is a precursor for food additives. Efficient electrochemical synthesis processes relying on low-carbon (e.g. wind) electricity have the potential to reduce this footprint by as much as one order of magnitude[4–6].

Today, direct CO_2RR strategies suffer from CO_2 crossover to the anode, leading to a large energy penalty from the associated CO_2 re-separation[7–9]. A cascade approach starting from a CO_2RR-to-CO process, followed by CORR-to-acetate, has seen encouraging progress and a reduced crossover penalty[10–15]. The realization of this technology for liquid hydrocarbon production hinges on improving electrochemical CORR performance e.g. faradaic efficiency (FE), partial current density ($J_{Partial}$) and full-cell energy efficiency (EE).

It is also imperative that liquid product mixtures – the combination of ethanol, acetate, and propanol, for example – be delivered at high concentrations. This is due to the high separation costs associated with low concentration electrolyte mixtures of liquid hydrocarbons (to illustrate: at concentrations below 1 wt.%, > 200 GJ $ton^{-1}_{Acetate}$ of purification energy cost are estimated to be incurred (Supplementary Table 1 and 2)). So far, the highest FEs to liquid products (either C_{2+} liquid hydrocarbon reaching 55%) and the highest concentrations of liquid products (1 wt.%) have yet to be united in a single high-FE high-concentration system[16,17]. Herein, we aim to combine

catalyst and system design to improve reaction kinetics while minimizing the liquid separation cost.

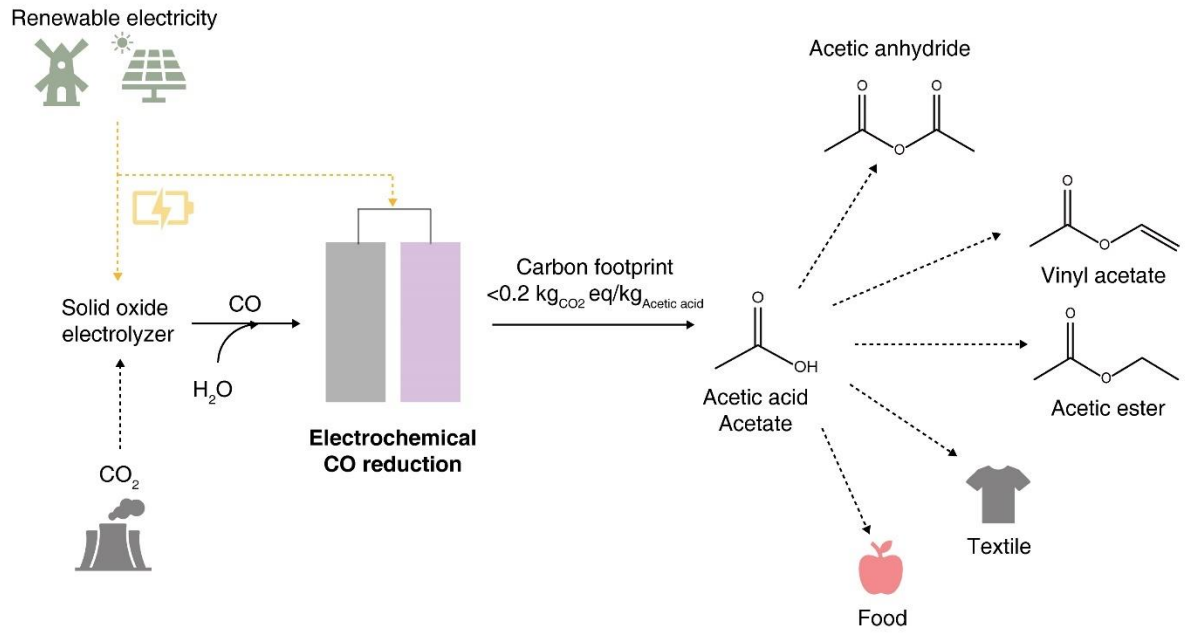

Scheme 1. Chemical product chain of acetic acid electrosynthesis

We posit a two-step acetic acid electrosynthesis approach and estimate that if high energy efficiency is reached – it would offer a ~ 10-fold reduction of GHG emissions when powered by low-carbon (wind, 6 gCO2e/kWhr) electricity and using CO_2 (or CO derived therefrom) as feedstock (Scheme 1).

The CORR-to-acetate step is most in need of improving, and thus we began, using DFT, to explore how AgCu at different Ag:Cu ratios could selectively destabilize key intermediates along the ethylene and ethanol pathway. We synthesized a series of Ag-Cu_2O catalysts using a kinetically restricted galvanic replacement strategy to vary surface Ag content, seeking to implement the active sites pointed to by DFT. Ag-Cu_2O catalysts reach acetate FE of 70% at

optimal Ag:Cu loading. We achieve a partial current density to acetate of 310 mA cm^{-2}. By implementing the catalyst in a membrane electrode assembly (MEA), we achieve a full cell energy efficiency (EE) of 25.5%, and this is accompanied by a sodium acetate concentration of 4.8 wt.%. Energy analysis over the full acetic acid production pathway shows a cascade system utilizing this CORR technology having an overall energy intensity of 93 GJ $ton^{-1}_{Acetate}$ (Supplementary Table 1 and 2): this compares encouragingly with 560 GJ ton^{-1} (CO_2RR, bipolar) and 300 GJ ton^{-1} (CO_2RR, neutral) and is a major step towards replacing current production methods.

Result and discussion

DFT calculations

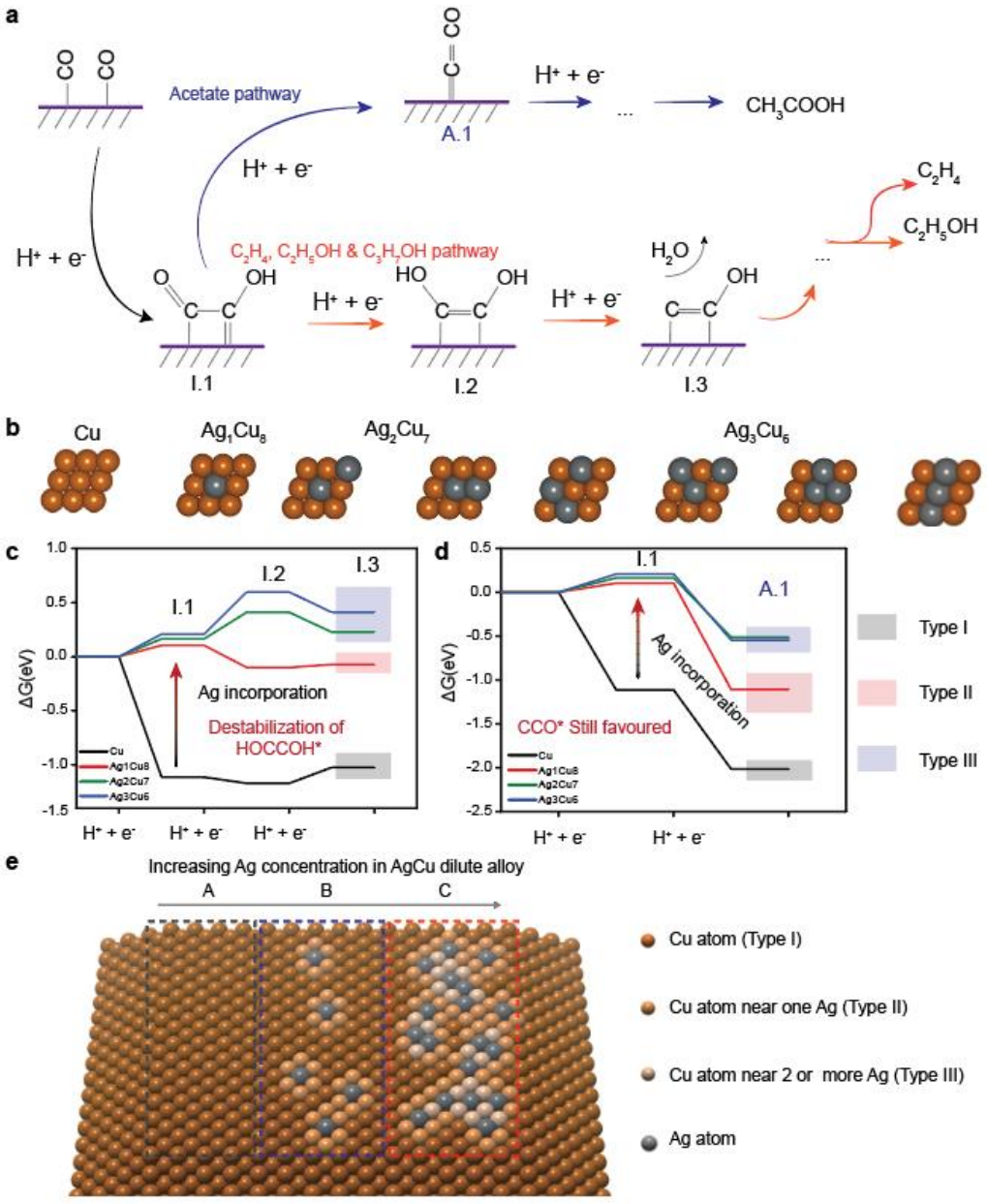

Figure 1. Computational studies of C_2 pathways on AgCu slabs. a, Reaction pathway for ethylene, ethanol and acetate production in CORR, where I.1 is OCCOH*, I.2 is HOCCOH*, I.3 is CCOH* and A.1 is CCO*. **b,** Different AgCu slabs used for simulating the reaction pathway of C_2 product in CORR. **c, d** Gibbs free energy change of the reaction pathway towards ethylene and ethanol through HOCCOH*, and

towards acetate through CCO* for different AgCu slabs. **e,** Effect of silver content in AgCu surface alloys giving rise to different active sites and their distribution.

Selective stabilization/destabilization of an intermediate along a product pathway can promote/suppress the selectivity toward a specific product during CORR. We start by investigating the difference in energetics of the ethylene and ethanol versus the acetate pathway on the C-C coupling active slab of Cu(100) (Figure 1). We find the most favorable pathway towards C-C coupling to go through OCCOH* (Figure 1a, intermediate I.1), with the subsequent proton-coupled electron transfer dictating the pathway towards either ethylene/ethanol via HOCCOH*, or acetate via CCO* (intermediate I.2 and A.1, respectively, Figure 1a)[18–21]. This points to HOCCOH* as the intermediate that diverges the ethanol-ethylene pathway from the acetate pathway. Controlled destabilization can thus usefully produce conditions wherein the HOCCOH* evolution is endergonic, while the CCO* remains exergonic.

Substitution of surface atoms with heteroatoms in bimetallic alloys modulates the electronic configuration of surrounding atoms. Ag has a lower CO* binding energy than Cu, and hence has the potential to destabilize all intermediates along the OCCOH* pathway. We simulate a series of AgCu surfaces with different Ag:Cu ratios (Figure 1b, Supplementary Figure 1-9) and re-calculate the energy along both pathways on these slabs (Figure 1c and d, Supplementary Table 3-10), along with the CO* adsorption energy (Supplementary Figure 10). We find that the addition of silver, even at 1Ag8Cu surface coverage destabilizes the HOCCOH* and CCO* pathways; however, both pathways remain exergonic and accessible. In higher Ag content cases of 2Ag7Cu and 3Ag6Cu, the HOCCOH* pathway becomes endergonic, while the CCO* pathways remain exergonic. It is in this regime of Ag:Cu ratio that we postulate one may suppress the formation of

ethylene and ethanol, while keeping the acetate pathway energetically accessible, suggesting a route to enhanced acetate FE.

We identify distinct reaction regimes, as a function of Ag content, and refer to their active sites as type I (pure copper), type II (one Ag neighbor, 1Ag8Cu) and type III (more than one Ag neighbor, 2Ag7Cu and 3Ag6Cu). Figure 1e shows the evolution of new active sites moving from I through II to III and the increase in their relative population with increased surface Ag content. Two factors control the intensity of the change in product distribution: 1) the electronic difference of the new active sites from the pure Cu sites 2) the relative distribution of these active sites versus the pure Cu sites. We targeted increasing, experimentally, the surface Ag atoms to the point where the type II and type III sites are dominant.

Synthesis and characterization of the Ag-Cu2O

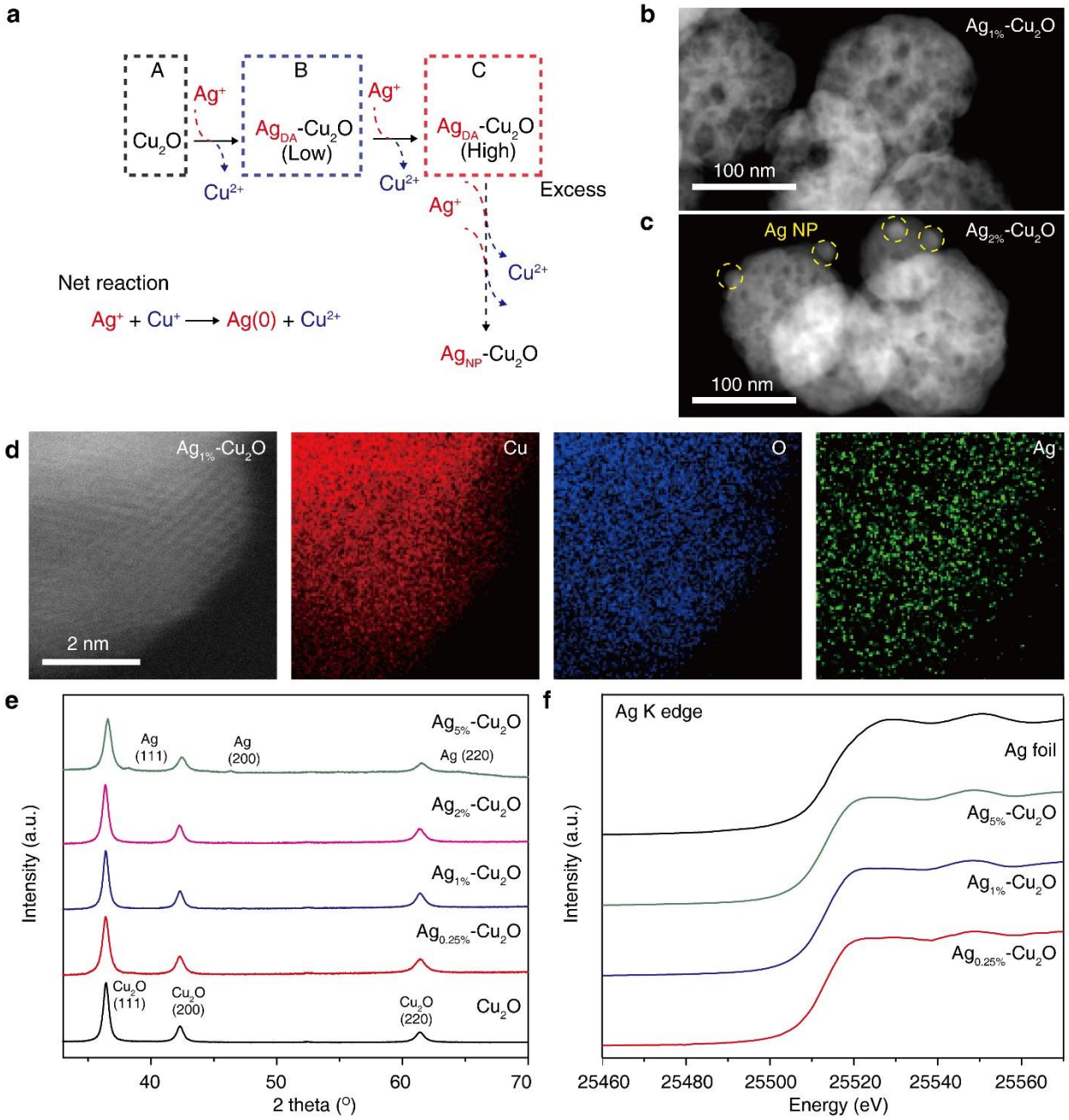

Figure 2. Synthesis and characterization of Ag-Cu2O catalysts. a, Synthetic scheme for AgCu bimetallic catalyst materials through galvanic replacement reaction. STEM image of **b,** $Ag_{1\%}$-Cu_2O and **c,** $Ag_{2\%}$-Cu_2O. **d,** High resolution Cs-corrected HAADF STEM-EDS image of $Ag_{1\%}$-Cu_2O catalyst showing uniform Ag distribution. **e,** XRD patterns and **f,** Ag K edge XANES spectra of AgCu bimetallic catalysts with different Ag concentrations.

Porous Cu_2O nanoparticles provide a platform for the control of surface Ag concentration within the pre-catalyst via galvanic replacement reaction. We synthesized porous Cu_2O nanoparticles and employed kinetically restricted galvanic replacement between Cu_2O and Ag^+ ions (Figure 2a) to tune the distribution of Ag on the surface. In contrast with previous reports that form Ag nanoparticles on the Cu surface during galvanic replacement[22], when we restrict replacement kinetics by controlling Ag precursor concentration in the reaction mixture, we produce uniformly dispersed Ag on the Cu_2O surface. Scanning transmission electron microscopy (STEM) shows ~100 nm sized porous Cu_2O nanoparticles initially lacking Ag nanoparticles up to an Ag concentration of 1% (Figure 2b, Supplementary Figures 11 and 12). When we introduce Ag beyond 1%, Ag nanoparticles do form (viz. 2% Ag, with 10-15 nm diameter Ag nanoparticle size, Figure 2c, Supplementary Figure 13-14), and these grow larger in the 5% Ag sample (50-60 nm, Supplementary Figure 15). EDS images of 2% and 5% Ag samples show that agglomerate particles on Cu surface are Ag nanoparticles. We then combined atomic resolution imaging high-angle annular dark-field (HAADF) STEM and EDS analysis using Cs-corrected STEM to visualize the Ag distribution on the Cu_2O surface (Figure 2d, Supplementary Figures 16-19). The presence of Ag NP larger than 0.5 nm was absent up to $Ag_{1\%}$-Cu_2O, with Ag NP formation being observed above this Ag loading. HAADF-STEM and EDS analysis on the Ag NP-free surface of $Ag_{2\%}$-Cu_2O confirms that Ag exist as two different species: 1) uniformly distributed Ag and 2) Ag NP, even when Ag NPs are formed. In X-ray diffraction (XRD), Ag metal peaks such as (111), (200) and (220) emerge above 2% Ag concentration (Figure 2e). Ag K edge X-ray absorption near-edge structure (XANES) fluorescence spectroscopy shows a characteristic metallic Ag absorption edge of 25520 eV indicating that Ag is in a metallic state for all Ag concentrations (Figure 2f)[23].

High-resolution X-ray photoelectron spectroscopy (XPS) indicates metallic Ag (Supplementary Figure 20). Cu K-edge XANES and EXAFS fluorescence spectra of the Ag-containing catalysts reveal that surface Cu in the unreacted electrodes is in the +1 oxidation state (Supplementary Figure 21 and 22).

CO electroreduction performance of Ag-Cu_2O

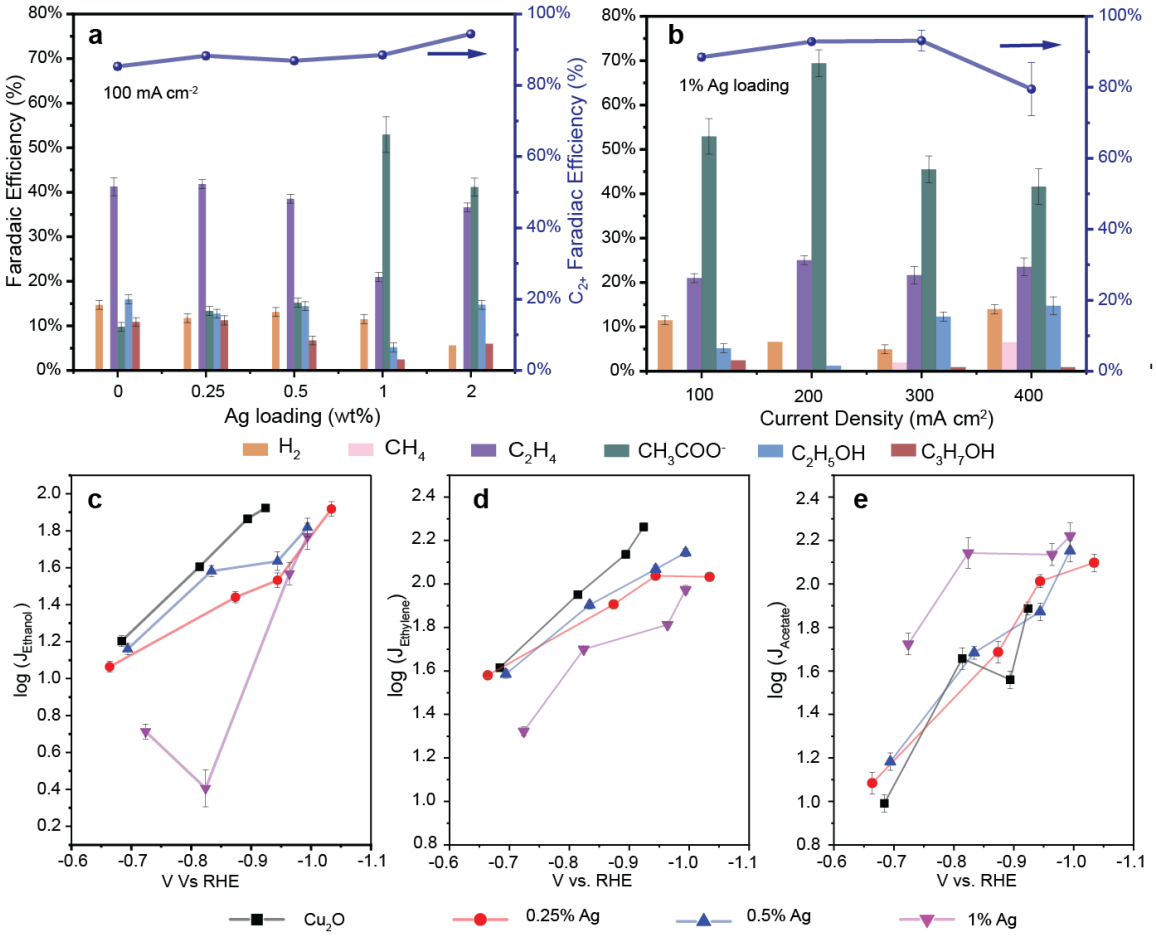

Figure 3. Electrochemical performance measurement of Ag-Cu_2O series. a, Faradaic efficiencies of hydrogen, methane, ethylene, acetate, ethanol and propanol during CO electroreduction at 100 mA cm^{-2} in a three-electrode flow cell. **b,** Faradaic efficiency distribution of CORR products for the $Ag_{1\%}$-Cu_2O at different current densities. **c, d, and e** (ethanol, ethylene, and acetate, respectively) Partial current densities of C_2 products for the Cu_2O and 0.25%, 0.5% and 1% Ag-Cu_2O catalysts.

We used a flow cell with a gas diffusion layer to study the electrocatalytic performance operating at >100 mA cm^{-2} current density (Supplementary Figure 23)[24]. The Ag-Cu_2O pre-catalysts reduce to metal Ag-Cu alloys under CORR condition (Supplementary Figure 35)[25]. We measured the electrochemical surface area (ECSA) of pure Cu_2O and $Ag_{1\%}$-Cu_2O following

chronopotentiometry at 100, 200, 300 and 400 mA cm^{-2} (Supplementary Figures 24 – 27). The ECSA reaches its maximum at higher potentials and remains high even when brought to a lower potential afterward (Supplementary Figure 28 and Supplementary Note 4). All CORR performance measurements are hence taken after the catalysts reach their highest ECSA.

Figure 3a shows the faradaic efficiencies of CORR for various Ag-Cu_2O samples at 100 mA cm^{-2} and 1M KOH. Pure Cu_2O-derived catalyst (referred to as Cu_2O from now on) show the lowest acetate FE of 10% and achieve a high C_{2+} FE of 85%. Oxide-derived copper enables C-C coupling from the abundance of grain boundaries formed during in-situ reduction[26–28]. Acetate productivity increases at the expense of hydrogen, ethylene, and ethanol, as the Ag concentration increases in the Ag-Cu_2O samples. The decrease in ethylene and hydrogen FE from 40 to 35% and 15 to 13% respectively, is accompanied by an increase in acetate from 10% to 15%. Increasing the Ag loading further to 1% illustrates the scarcity of type II /III sites at 0.5%, as there is a sudden and dramatic change in the FE distribution. The ethylene is reduced to ~22% with a sharp increase in acetate to 55%. Increasing Ag loading to 1% transforms type I sites to type II and III (Figure 1e), to the point where the average FE reflects a completely new distribution of active sites and their intrinsic activities. To probe the best Ag loading at which the type II/III active sites are maximized, we tested a 2% Ag loading sample. At this loading, agglomerated Ag NPs are observed (Figure 2c, Supplementary Figure 11). This is reflected in the FE distribution with ethylene and ethanol FE starting to increase, and acetate formation being suppressed. Supplementary Figure 29 shows the FE distribution of all Ag-Cu_2O samples at 100, 200, 300 and 400 mA cm^{-2}, while the performance of a commercial CuAg alloy catalyst is shown to produce >50% FE towards H_2 (Supplementary Figure 30).

The potential dependence of the $Ag_{1\%}$-Cu_2O sample FE is shown in Figure 3b. Increasing the current density from 100 mA cm^{-2} to 200 mA cm^{-2} causes FE to C_{2+} products to increase. This is accompanied by a drop in the hydrogen evolution reaction (HER) FE, with no increase in CH_4 FE. At this current density, the C_2 product distribution shifts towards higher acetate, peaking at an FE of 70%. Further increase of the current density results in the increase of ethanol. It is also at this potential that CH_4 formation reaches detectable limits, an indication of depletion of the surface CO. This is confirmed by the increase in CH_4 and HER at 400 mA cm^{-2} and a decrease in C_{2+}. We probe the effect of Ag loading close to the 1% optimum (Supplementary Figure 31) with 0.25% increments and find that 1% shows the highest acetate FE at 100 and 200 mA cm^{-2}, confirming that at this loading the typ II/III sites are maximized. The FE to acetate remains high at large current density with a peak $J_{acetate}$ of 310 mA cm^{-2} (Supplementary Figure 32).

Figures 3c, d and e show the partial current densities of the C_2 products vs. half-cell potentials (iR-corrected). The ethylene and ethanol partial current density of the 0.25% and 0.5% Ag samples are below that of Cu_2O, showing that at low surface coverages, silver acts as an inhibitor to these product pathways. In the 1%Ag sample, the same inhibitory trend of $J_{Ethylene}$ continues and reaches its lowest value. In the case of ethanol, this inhibition is exaggerated at lower potentials (Figure 3c). This is due to the abundance of type II/III sites which destabilize the ethanol pathway to a point where larger reductive potentials are needed to enable access to this pathway.

The partial current density of acetate remains relatively unchanged across all silver loadings. This shows that increasing the number of type II/III active sites does not enhance the production rate of acetate, but it inhibits competing product pathways, enhancing reaction selectivity towards acetate. In the 1%Ag sample, there is a slight increase in $J_{Acetate}$ at lower

potentials (Figure 3e). This is attributed to a decrease in the hydrogen evolution reaction (HER) at those potential ranges, which result in more J_{C2} and by extension a higher $J_{Acetate}$. At higher potentials (< -0.9 Vs RHE) the $J_{Acetate}$ of the 1%Ag becomes equal to those of its lower Ag loading counterparts.

Operando and post-catalysis characterizations

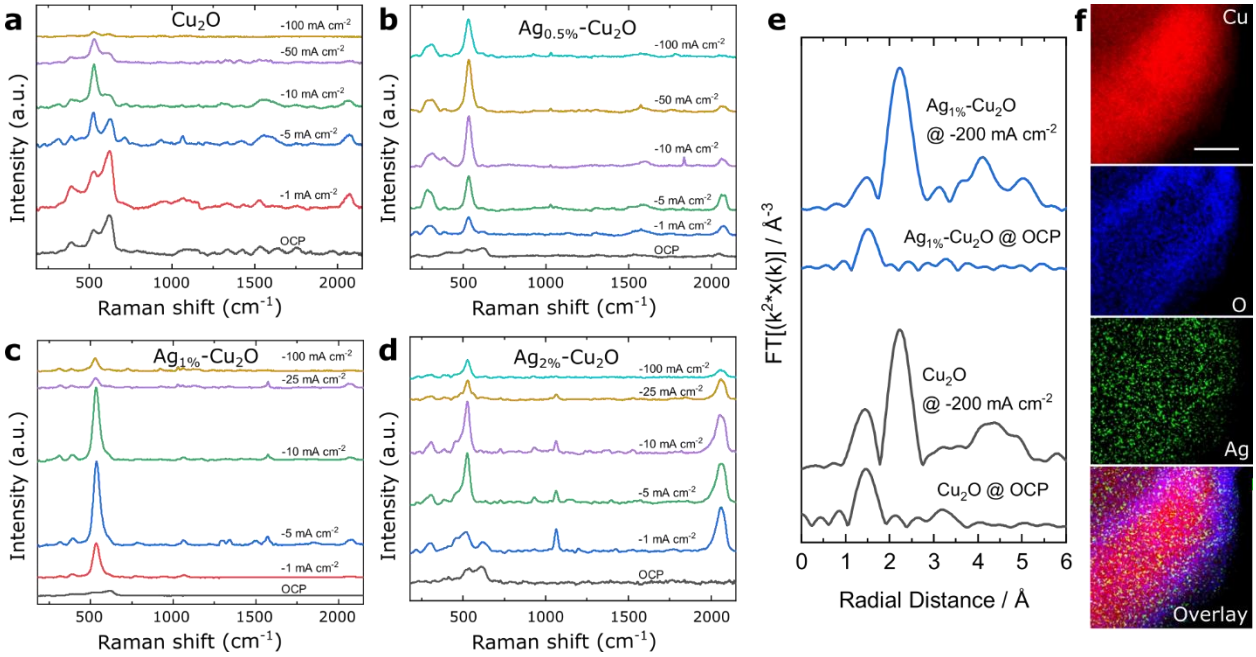

Figure 4. a-d, *operando* Raman spectroscopy studies of Cu_2O, $Ag_{0.5\%}$-Cu_2O, $Ag_{1\%}$-Cu_2O and $Ag_{2\%}$-Cu_2O $Ag_{x\%}$-Cu_2O, respectively in a flow cell with the electrodes in contact with 1 M KOH. The spectra are collected in chronopotentiometry mode. **e**, operando Cu K-edge EXAFS of Cu_2O and $Ag_{1\%}$-Cu_2O spectra collected before starting CORR and under CORR at –200 mA cm^{-2}. **f**, HR-TEM with elemental EDX mapping at atomic resolution (scale bar is 10 nm) of a $Ag_{1\%}$-Cu_2O after CORR.

We used *operando* Raman spectroscopy to interrogate the surface species during CORR under different potentials and identify the bound intermediates leading to C_{2+} products at a molecular level[29]. As we step the current below -1 mA cm^{-2} (Figure 4a-d), the Cu oxides peaks disappear (Figure 4a-d and Supplementary Figure 33), and the broad feature of atop-bound CO* peaking at 2065 cm^{-1} appears. The signal intensity under low current densities (-5 mA cm^{-2}) is

representative of the CO* saturation coverage[30]. At this current density, the presence of type II/III active sites when few silver atoms are on the surface in $Ag_{0.5\%}$-Cu_2O increases the *CO coverage, and two new adsorption modes appear: Cu-CO frustrated rotation (the broad feature of peaking at 290 cm^{-1}) and a new peak of atop Ag-CO (the sharp peak at 535 cm^{-1})[23,31–34]. With more type II/III sites in $Ag_{1\%}$-Cu_2O, the Cu-CO frustrated rotation feature is more defined and associated with the Cu-CO stretching signal at 380 cm^{-1}. In the Raman spectra the bands of Cu-CO frustrated rotation and stretching are shifted to higher frequency compared to literature values. The shift indicates a stronger Cu-CO bond which may favor C-C coupling[35,36]. Larger Ag amounts (e.g. 2%) increase atop-bound CO*, peaking at 2065 cm^{-1} and the sharp Ag-CO peak at 535 cm^{-1} shows a shoulder at 480 cm^{-1} associated with adsorbed CO on bulk Ag of silver nanoparticles[32].

We observe additional sharp bands in the 700-1600 cm^{-1} region when type II/III active sites are available at Ag above 1%. Control experiments with argon show that these peaks to arise during CORR (Supplementary Figure 34). These Raman modes are associated with acetate-specific intermediates e.g., vibration modes of carboxylate (COO^-) and other C_2 intermediates (Supplementary Figure 35)[29,37–39]. Their intensification indicates larger abundance of stabilized acetate intermediates on $Ag_{1\%}$-Cu_2O and $Ag_{2\%}$-Cu_2O as the number of type II/III sites increases. Atop CO* is a key species toward C_{2+}, and the additional coverage of Ag-CO favors high selectivity toward C_{2+}.[40] As we stepped to more negative current densities, the intensity of the adsorbed intermediates decreased due to their progressive consumption and the formation of the bubbles.

We performed *operando* X-ray absorption experiments to investigate the local electronic nature of the catalysts during CORR. Operando XANES on the Cu K-edge in the Cu_2O and Ag1%-

Cu_2O samples indicate that the copper is in the metallic state during CORR (Supplementary Figure 36). Operando EXAFS shows that the local structure of Cu is unaltered by the presence of surface Ag, which we attribute to the large Cu to Ag ratio in catalysts. We examined the spent $Ag_{1\%}$-Cu_2O catalyst with HAADF-STEM with EDS mapping after CORR (Figure 4f, Supplementary Figure 37 and 38). After CORR the Ag is still uniformly distributed on Cu_2O surface without signs of agglomeration. Moreover, oxygen is now distributed at the surface, as seen by the blue right edge of the nanoparticle, confirming that during CORR the Cu_2O undergoes reduction followed by surface oxidation in the air after we turned off the reaction.

These spectroscopic observations reveal that the presence of surface Ag atoms on Cu_2O allows modulation of the adsorption of CORR intermediates by regulating Ag loading. The presence of new active sites promotes surface CO dimerization by suppressing the competing HER reaction, and the preferential destabilization of intermediates along the ethylene and ethanol pathway promote acetate selectivity through the *CCO intermediate as supported by the DFT study. Operando XAS and EDX mapping on spent samples show that the catalyst retains its atomic-scale architecture during catalysis.

Membrane electrode assembly systems for concentrated sodium acetate production

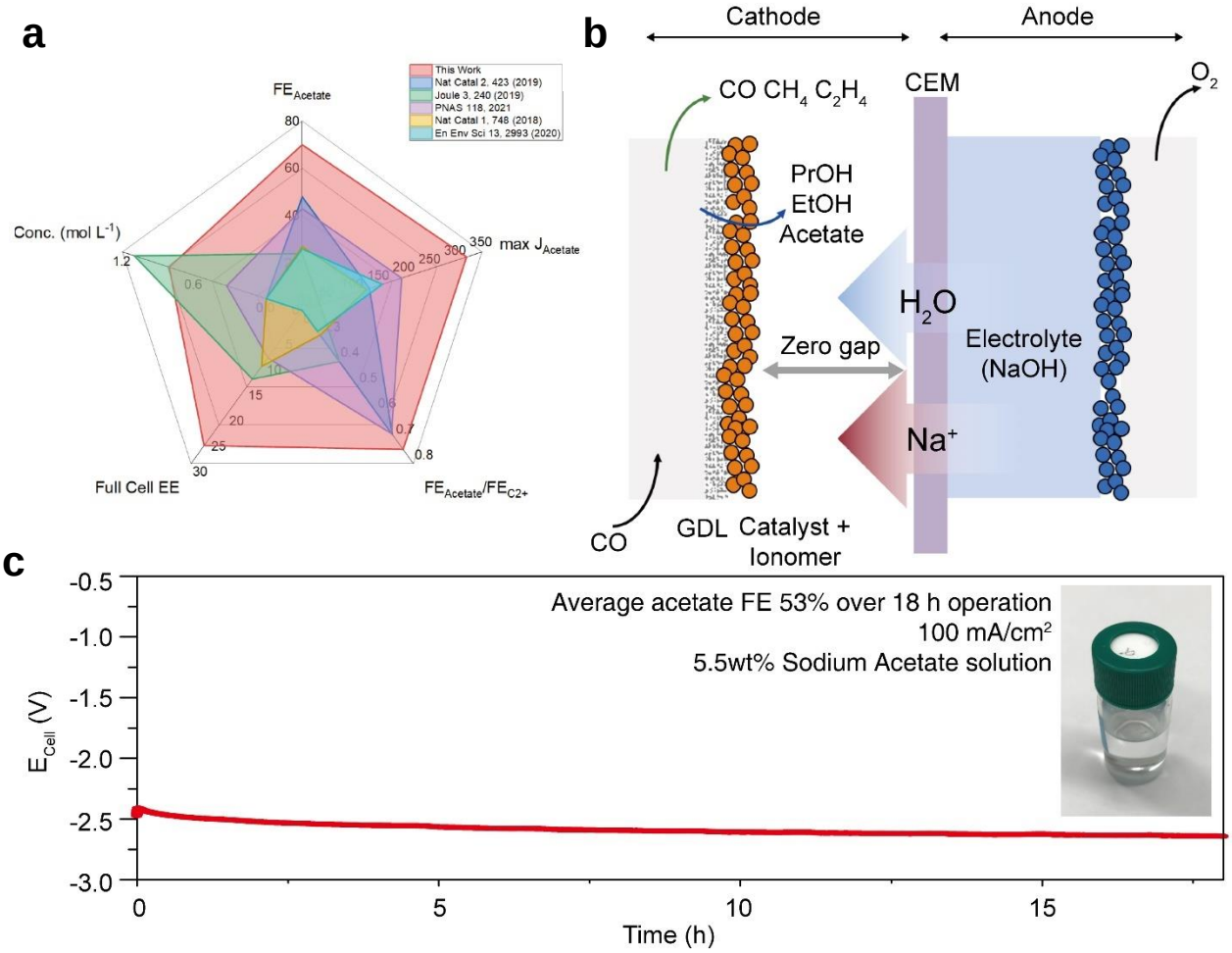

Figure 5. Acetate production activity of Ag-Cu_2O catalyst and concentrated acetate production in MEA application. a, Comparison of performance metrics of this work and other relevant references. **b,** Schematic image of MEA application. **c,** Chronopotentiometry stability test of $Ag_{1\%}$-Cu_2O at 100 mA/cm^2 in MEA with a product concentration of 5.5 wt.% (0.9M).

We further demonstrate the applicability of the catalyst in a zero-gap MEA similar to that used by Ripatti et al[17]. Recent studies by Wang et al have highlighted the importance of product concentration in CO_2RR and CORR[41]. However, minimization of the electrical energy input in a CORR system is needed due to the preceding CO_2-to-CO endothermic step when compared to

direct CO_2RR. Therefore, the targets of liquid concentration and low full cell voltage at industrially relevant current densities need to be met within the same system. Figure 5a compares performance herein (both flow cell and MEA) with prior work. The Ag-Cu_2O catalyst exhibits the highest acetate FE reported, and it shifts the C_2 product pathway to acetate ($FE_{acetate}/FE_{C2}$) (Supplementary Table 10). Using a zero-gap system of Figure 5b and circulating 1M NaOH solution as anolyte enabled a ~4.8 wt.% sodium acetate solution with stable operation over 18 hours at 2.5 V full cell potential and 100 mA cm^{-2} (Figure 5c). This corresponds to a full cell energy efficiency of 25.5%[41,42].

Conclusion

In this work we demonstrate a two-step electrosynthesis process for the production of acetic acid with a 10-fold lower carbon footprint. The family of Ag-Cu_2O alloy nanoparticle precatalysts with different Ag loadings enabled inhibition, *operando*, of the formation of ethylene and ethanol, resulting in an acetate FE of 70% FE at 200 mA cm^{-2}. Computational studies, electrochemical measurements, and *operando* Raman spectroscopy elucidate the role of Ag incorporation onto Cu in selective acetate production. We provide evidence that the presence of Ag and the active sites surrounding Ag atoms destabilizes the ethanol and ethylene pathway in CORR while maintaining the exergonicity of the acetate pathway. The optimized catalyst can produce a peak acetate FE of 70% at 200 mA cm^{-2}. The catalyst in a zero-gap MEA system enables ~5 wt.% sodium acetate solution over 18 hours of stable operation with a full cell EE of 25.5% at 100 mA cm^{-2}.

Methods

Preparation of catalyst and gas diffusion electrode

Materials

$Cu(CH_3COO^-)_2$, aqueous N_2H_4 solution (35 wt.%), $AgNO_3$, ethanol, HCl (37 wt.%), KOH, dimethyl sulfoxide, deuterated water (D_2O), PTFE nanoparticles (Nanoshel, 350-400 nm), and methanol, were used as purchased from Aldrich. Carbon monoxide (grade 4) was purchased from Praxair and Ar (grade 5) was purchased from Messer. Nickel foam was purchased from MTI Corporation. Carbon-based gas diffusion electrode (Freudenberg H23C9), anion exchange membrane (Fumasep FAA-PK-130), Nafion 212, 5% Nafion perfluorinated resin solution 5 wt. % (D520 EW=1000) were purchased from the Fuel Cell store. Deionized water (18.2 MΩ) was used in all experiments.

Synthesis of electrocatalysts

Synthesis of Ag-Cu_2O catalysts with various concentrations followed a two-step procedure [43]. The first step is the synthesis of porous Cu_2O nanoparticles, modified from a previously reported method. 200 mg of $Cu(CH_3COO^-)_2$ H_2O were dissolved in 80 ml H_2O. 300 ul of 35 wt.% N_2H_4 solution was added dropwise to the aqueous Cu acetate solution. Note that N_2H_4 solution is a strong reductant and should be added very slowly, and Cu acetate solution should be vigorously stirred to prevent agglomerated Cu nanoparticle formation. 1 ml of 2 M HCl solution was added dropwise to the reaction mixture and magnetically stirred for 30 min. The reaction mixture was centrifuged and washed with water and ethanol twice to obtain porous Cu_2O nanoparticle. The second step is

a kinetically controlled galvanic replacement reaction between Cu_2O and Ag^+ cation. Porous Cu_2O nanoparticle was dispersed in 30 ml H_2O. Aqueous $AgNO_3$ solution of 1 mg/ml concentration is prepared. The calculated amount of $AgNO_3$ solution (for example, 0.98 ml for 1%) is slowly dropwise for 2 h into vigorously stirred aqueous Cu_2O solution. The reaction mixture was vigorously stirred for an additional 30 min. The reaction mixture was washed in water and lyophilized to obtain final Ag-Cu_2O catalysts.

Preparation of gas-diffusion electrode

The catalyst was deposited on a Freudenberg H23C9 (Fuel Cell Store) gas diffusion electrode using an airbrush technique, with GDE dimensions of (3 x 3 cm^2) or (2 x 2 cm^{-2}). The ink was composed of the catalyst nanoparticles (Cu_2O and Ag-Cu_2O), 5% Nafion solution (Fuel Cell Store D520, EW=1000), PTFE nanoparticles (Nanoshel, 350-400 nm) and 5 ml of methanol (Sigma Aldrich). The ink composition was chosen to obtain a 0.8 mg cm^{-2} catalyst loading with a Nafion content of 40 μl_{Nafion} : 1 $mg_{Catalyst}$ and a PTFE content of 1 $mg_{PTFE\ NP}$: 1 $mg_{Catalyst}$. The ink was vortexed for 5 minutes and sonicated for more than 1 hour before being deposited on the GDE. For the electrode samples used in the MEA setup, the PTFE nanoparticles were omitted from the ink composition. The electrode was left in room conditions overnight before being conducting electrochemical measurements.

Structural characterization

TEM imaging was conducted on a JEOL EM-2010 microscope operated at 200 kV. STEM imaging and EDS measurements were performed STEM mode equipped with a single drift detector (X-MAX^N Oxford Instruments). SEM imaging was conducted on a Hitachi FE-SEM SU5000 microscope operated at 30 kV. The powder samples were deposited on a carbon tape before SEM

imaging. XRD analysis was performed on a MiniFlex600 system employing Cu Kα radiation. XPS measurements were conducted using the PerkinElmer model 5600, equipped with 1,486.6 eV monochromated Al Kα X-ray source. The samples were prepared on conductive glass substrates by drop-casting a few droplets of ink solution.

High-resolution transmission electron microscopy measures at the atomic scale were carried out at the ScopeM facility ETH-Zurich by employing a JEOL JEM-ARM300F Grand ARM "Vortex“ operated at 200 kV in STEM mode. EDS mapping was performed on dual large-area SDD EDX detectors with 100 mm^2 active area; total solid angle: 1.6 sr and energy resolution: ≤ 133 eV for Mn-Kα. The ABF (annular bright field) inner and outer semi-angle were set to 12 and 24 mrad, respectively. HAADF inner and outer semi-angle were set to 64 and 180 mrad, respectively.

Electrochemical CO reduction measurements

Electrochemical rate measurements were performed in both a flow cell and membrane electrode assembly (MEA) configuration. For the flow cell setup, the catalyst deposited GDE was used as the working electrode (cathode) and nickel foam (MTI Corporation) as the counter electrode (anode). An anion exchange membrane (Fumasep FAA-PK-130) was used to separate the anodic and cathodic compartments. The flow cell assembly constituted the GDE, anion exchange membrane, and nickel anode, while liquid electrolyte (1M KOH, Sigma Aldrich) was circulated in both anodic and cathodic compartments using a peristaltic pump (McMaster-Carr). Carbon monoxide (Praxair, Grade 4.0) was passed behind the GDE using a mass flow controller (Sierra SmartTrack 100), while an Ag/AgCl reference electrode was inserted inside the cathodic compartment for half-cell potential measurement. For the MEA setup, the catalyst-deposited GDE

was used as the working electrode (cathode) and an IrO_2-Ti felt (Sigma Aldrich) as the anode. A Nafion 212 (Fuel Cell Store) cation-exchange membrane was used to keep a separation between the anolyte and the cathodic liquid products. The MEA was assembled by layering the GDE, Nafion and IrO_2-Ti felt and pressing them between the cathode plate (1 cm^2 flow field, stainless steel) and the anode plate (5 cm^2 titanium, flow field). A 1M NaOH solution was circulated through the anodic flow field using a peristaltic pump, while carbon monoxide was flown into the cathodic flow field using a mass flow controller. The liquid products were collected inside a cooled container (2-6°C) from the outlet of the cathode plate. For both configurations, the carbon monoxide flowrate was 25-40 standard cubic centimeters per minute (SCCM), and the electrolyte flow was 10-15 ml min^{-1}. Electrochemical reactions were performed using an electrochemical workstation (Autolab PGSTAT302N) connected to a current booster (Metrohm Autolab, 10 A). Electrode potentials were rescaled to the RHE reference by:

$$E_{Vs\ RHE} = E_{Vs\ Ag/AgCl} + 0.235V + 0.059 \times PH$$

An electrochemical impedance spectroscopy (EIS) measurement using an Autolab PGSTAT302N electrochemical workstation was performed to obtain a cell resistance of 3.51 Ω. iR corrections to the potential were then performed using the following equation:

$$E_{iR-free} = E_{Vs\ Ag/AgCl} - 0.85R_{cell}i_{cell}$$

Where $E_{iR\text{-}free}$ is the corrected potential at the cathode, $E_{Vs\ Ag/AgCl}$ is the applied potential, and i_{cell} is the total current (a negative value at the cathode). A correction factor of 0.85 is used due to the 1 M KOH electrolyte's high conductance and low voltage drop across the electrolyte.

The full-cell energy efficiency of the MEA system is obtained from the following equation:

$$EE_{Full-cell} = FE_{Acetate} * \frac{E^0_{cell}}{V_{Full-cell}}$$

Where $EE_{Full\text{-}cell}$ is the full-cell energy efficiency of the system, $FE_{Acetate}$ is the system's faradaic efficiency towards acetate, and $V_{Full\text{-}cell}$ is the average full cell voltage over the length of the stability experiment. The standard reduction potential of the cell is obtained from the standard Gibbs free energy of the reaction $2CO + 2H_2O \rightarrow CH_3COOH + 2O_2$:

$$E^0_{cell} = \frac{-\Delta G^0_{2CO+2H2O \rightarrow Acetate+2O2}}{zF}$$

Where z is equal to 4 and F is the faraday constant 96485 C mol^{-1}.

Product analysis

The gas products from CORR were analyzed by sampling 1ml of the Electrolyzer outlet gas with an air-tight syringe (Hamilton, 5 ml). The gas sample was injected into a gas chromatograph (Shimadzu GC-2014) equipped with a thermal conductivity detector (TCD) and a flame ionization detector (FID). A Molecular Sieve 5A and Carboxen-1000 column were installed upstream from the TCD and FID respectively to separate the H_2, CO and gaseous hydrocarbons. The liquid products were quantified using nuclear magnetic resonance spectroscopy (NMR) and high-performance liquid chromatography (HPLC). A 1ml sample of the electrolyte was taken at various times during the reaction. 1H NMR spectra of the analyte samples were taken using an Agilent DD2 600 spectrometer with dimethyl sulfoxide (DMSO) as an internal standard. For accurate measurement of the acetate concentration, an HPLC equipped with a HPX87H Aminex column (Bio-Rad) was calibrated for acetate. The results from both the HPLC and NMR were within 5% error. Faradaic efficiency (FE) of CORR gas product was calculated by the following equation:

$$FE_{i,gas} = y_{i,g} \dot{V} z_i F \frac{P_0}{RT} j_{total}$$

Where y_i is the volume fraction of gas product i, V is the outlet gas flow rate in sccm, z_i is the number of electrons associated with producing one molecule of i, F is the Faraday constant, P_0 is atmospheric pressure, R is the ideal gas constant, T is the temperature and j_{total} is the total current density. The FE of liquid product was calculated using the following equation:

$$FE_{i,liquid} = n_{i,liquid} z_i F \frac{1}{Q_{total}}$$

Where n_i is the number of moles of liquid product i, and Q is the total charge passed prior to the liquid sample being taken.

Electrochemical characterization

Cyclic voltammetry characterization with electrodes assembled in a flow cell was performed with the same equipment used for CORR experiments. iR correction of the applied potential was not performed.

***Operando* and *ex situ* spectroscopic analysis**

Operando and *ex situ* XAS Cu K-edge measurements were carried out at the European Synchrotron Radiation Facility (ESRF) at beamline ID26 which is equipped with high energy resolution fluorescence detectors (HERFD). We used a flow cell electrolyzer modified to host a X-ray transparent window facing the cathode backside. Ag K-edge and Cu K-edge experiments were conducted at beamline 9MB of the Advanced Photon Source at the Argonne National Laboratory and the Canadian Light Source.

Operando Raman was operated with a water immersion objective using a Renishaw inVia Raman microscope. The spectra were collected using 785 nm laser. To avoid damaging the samples, the full spectrum was collected in two ranges (centered at 700 and 1700 cm^{-1}) using 0.05% full laser intensity, 0.1s integration time, and 200 repetitions. The raw data were base corrected manually by using Origin 2019 software. An open-structured flow cell was utilized for the measurements. An Ag/AgCl electrode (filled with saturated aqueous KCl solution) and a platinum wire were used as the reference and counter electrode, respectively. We collected the spectra at different current densities per each catalyst to allow a comparison between the different Ag %, which is free of differences due to mass transport phenomena of surface species.

Computational methods

All DFT calculations in this work were carried out using a periodic slab model with the Vienna ab-initio simulation program (VASP) (https://www.vasp.at/). The supplementary information provides detailed information on the calculations and the derivation of the Gibbs free energy for elementary steps.

References

1. Schiffer, Z. J. & Manthiram, K. Electrification and Decarbonization of the Chemical Industry. *Joule* **1**, 10–14 (2017).

2. Luderer, G. *et al.* Impact of declining renewable energy costs on electrification in low-emission scenarios. *Nature Energy 2021* 1–11 (2021) doi:10.1038/s41560-021-00937-z.

3. Tackett, B. M., Gomez, E. & Chen, J. G. Net reduction of CO2 via its thermocatalytic and electrocatalytic transformation reactions in standard and hybrid processes. *Nature Catalysis 2019 2:5* **2**, 381–386 (2019).

4. Berre, C. le, Serp, P., Kalck, P. & Torrence, G. P. Acetic Acid. *Ullmann's Encyclopedia of Industrial Chemistry* 1–34 (2014) doi:10.1002/14356007.A01_045.PUB3.

5. Medrano-García, J. D., Ruiz-Femenia, R. & Caballero, J. A. Revisiting Classic Acetic Acid Synthesis: Optimal Hydrogen Consumption and Carbon Dioxide Utilization. *Computer Aided Chemical Engineering* **46**, 145–150 (2019).

6. Sodium Acetate Market Size, Shares & Industry Analysis | Research Report 2026. https://dataintelo.com/report/sodium-acetate-market/.

7. Alerte, T. *et al.* Downstream of the CO2Electrolyzer: Assessing the Energy Intensity of Product Separation. *ACS Energy Lett* **6**, 4405–4412 (2021).

8. Mardle, P., Cassegrain, S., Habibzadeh, F., Shi, Z. & Holdcroft, S. Carbonate Ion Crossover in Zero-Gap, KOH Anolyte CO2Electrolysis. *Journal of Physical Chemistry C* **125**, 25446–25454 (2021).

9. Rabinowitz, J. A. & Kanan, M. W. The future of low-temperature carbon dioxide electrolysis depends on solving one basic problem. *Nature Communications 2020 11:1* **11**, 1–3 (2020).

10. Zhang, X., Song, Y., Wang, G. & Bao, X. Co-electrolysis of CO2 and H2O in high-temperature solid oxide electrolysis cells: Recent advance in cathodes. *Journal of Energy Chemistry* **26**, 839–853 (2017).

11. Ramdin, M. *et al.* Electroreduction of CO 2 /CO to C 2 Products: Process Modeling, Downstream Separation, System Integration, and Economic Analysis . *Ind Eng Chem Res* **60**, 17862–17880 (2021).

12. Wang, L. *et al.* Power-to-fuels via solid-oxide electrolyzer: Operating window and techno-economics. *Renewable and Sustainable Energy Reviews* **110**, 174–187 (2019).

13. Gurudayal, G. *et al.* Sequential Cascade Electrocatalytic Conversion of Carbon Dioxide to C-C Coupled Products. *ACS Appl Energy Mater* **2**, 4551–4559 (2019).

14. Jouny, M., Luc, W. & Jiao, F. High-rate electroreduction of carbon monoxide to multi-carbon products. *Nature Catalysis 2018 1:10* **1**, 748–755 (2018).

15. Romero Cuellar, N. S. *et al.* Two-step electrochemical reduction of CO2 towards multi-carbon products at high current densities. *Journal of CO2 Utilization* **36**, 263–275 (2020).

16. Zhu, P. *et al.* Direct and continuous generation of pure acetic acid solutions via electrocatalytic carbon monoxide reduction. *Proc Natl Acad Sci U S A* **118**, (2021).

17. Ripatti, D. S., Veltman, T. R. & Kanan, M. W. Carbon Monoxide Gas Diffusion Electrolysis that Produces Concentrated C2 Products with High Single-Pass Conversion. *Joule* **3**, 240–256 (2019).

18. Santatiwongchai, J., Faungnawakij, K. & Hirunsit, P. Comprehensive Mechanism of CO2Electroreduction toward Ethylene and Ethanol: The Solvent Effect from Explicit Water-Cu(100) Interface Models. *ACS Catal* **11**, 9688–9701 (2021).

19. Calle-Vallejo, F. & Koper, M. T. M. Theoretical Considerations on the Electroreduction of CO to C2 Species on Cu(100) Electrodes. *Angewandte Chemie International Edition* **52**, 7282–7285 (2013).

20. Wang, L. *et al.* Electrochemical Carbon Monoxide Reduction on Polycrystalline Copper: Effects of Potential, Pressure, and pH on Selectivity toward Multicarbon and Oxygenated Products. *ACS Catal* **8**, 7445–7454 (2018).

21. Garza, A. J., Bell, A. T. & Head-Gordon, M. Mechanism of CO2 Reduction at Copper Surfaces: Pathways to C2 Products. *ACS Catal* **8**, 1490–1499 (2018).

22. Herzog, A. *et al.* Operando Investigation of Ag-Decorated Cu2O Nanocube Catalysts with Enhanced CO2 Electroreduction toward Liquid Products. *Angewandte Chemie International Edition* **60**, 7426–7435 (2021).

23. Herzog, A. *et al.* Operando Investigation of Ag-Decorated Cu2O Nanocube Catalysts with Enhanced CO2 Electroreduction toward Liquid Products. *Angewandte Chemie International Edition* **60**, 7426–7435 (2021).

24. García de Arquer, F. P. *et al.* CO2 electrolysis to multicarbon products at activities greater than 1 A cm−2. *Science (1979)* **367**, 661–666 (2020).

25. Lee, S. H. *et al.* Oxidation State and Surface Reconstruction of Cu under CO2Reduction Conditions from in Situ X-ray Characterization. *J Am Chem Soc* **143**, 588–592 (2021).

26. Verdaguer-Casadevall, A. *et al.* Probing the Active Surface Sites for CO Reduction on Oxide-Derived Copper Electrocatalysts. *J Am Chem Soc* **137**, 9808–9811 (2015).

27. Li, C. W., Ciston, J. & Kanan, M. W. Electroreduction of carbon monoxide to liquid fuel on oxide-derived nanocrystalline copper. *Nature* **508**, 504–507 (2014).

28. Wang, L. *et al.* Electrochemically converting carbon monoxide to liquid fuels by directing selectivity with electrode surface area. *Nature Catalysis 2019 2:8* **2**, 702–708 (2019).

29. Chernyshova, I. v., Somasundaran, P. & Ponnurangam, S. On the origin of the elusive first intermediate of CO2 electroreduction. *Proc Natl Acad Sci U S A* **115**, E9261–E9270 (2018).

30. Gunathunge, C. M., Ovalle, V. J., Li, Y., Janik, M. J. & Waegele, M. M. Existence of an Electrochemically Inert CO Population on Cu Electrodes in Alkaline pH. *ACS Catal* **8**, 7507–7516 (2018).

31. Oda, I., Ogasawara, H. & Ito, M. Carbon Monoxide Adsorption on Copper and Silver Electrodes during Carbon Dioxide Electroreduction Studied by Infrared Reflection Absorption Spectroscopy and Surface-Enhanced Raman Spectroscopy. *Langmuir* **12**, 1094–1097 (1996).

32. Gao, J. *et al.* Selective C-C Coupling in Carbon Dioxide Electroreduction via Efficient Spillover of Intermediates As Supported by Operando Raman Spectroscopy. *J Am Chem Soc* **141**, 18704–18714 (2019).

33. Li, J. *et al.* Constraining CO coverage on copper promotes high-efficiency ethylene electroproduction. *Nature Catalysis 2019 2:12* **2**, 1124–1131 (2019).

34. Shan, W. *et al.* In Situ Surface-Enhanced Raman Spectroscopic Evidence on the Origin of Selectivity in CO2Electrocatalytic Reduction. *ACS Nano* **14**, 11363–11372 (2020).

35. Fielicke, A., Gruene, P., Meijer, G. & Rayner, D. M. The adsorption of CO on transition metal clusters: A case study of cluster surface chemistry. *Surf Sci* **603**, 1427–1433 (2009).

36. Sandberg, R. B., Montoya, J. H., Chan, K. & Nørskov, J. K. CO-CO coupling on Cu facets: Coverage, strain and field effects. *Surf Sci* **654**, 56–62 (2016).

37. Quilès, F. & Burneau, A. Infrared and Raman spectra of alkaline-earth and copper(II) acetates in aqueous solutions. *Vib Spectrosc* **16**, 105–117 (1998).

38. Bohra, D. *et al.* Lateral Adsorbate Interactions Inhibit HCOO− while Promoting CO Selectivity for CO2 Electrocatalysis on Silver. *Angewandte Chemie* **131**, 1359–1363 (2019).

39. Shao, F. *et al.* In situ spectroelectrochemical probing of CO redox landscape on copper single-crystal surfaces. *Proc Natl Acad Sci U S A* **119**, e2118166119 (2022).

40. Li, F. *et al.* Molecular tuning of CO2-to-ethylene conversion. *Nature 2019 577:7791* **577**, 509–513 (2019).

41. Zhu, P. & Wang, H. High-purity and high-concentration liquid fuels through CO2 electroreduction. *Nature Catalysis 2021 4:11* **4**, 943–951 (2021).

42. Zhu, P. *et al.* Direct and continuous generation of pure acetic acid solutions via electrocatalytic carbon monoxide reduction. *Proc Natl Acad Sci U S A* **118**, (2021).

43. Yang, P. P. *et al.* Protecting Copper Oxidation State via Intermediate Confinement for Selective CO2 Electroreduction to C2+ Fuels. *J Am Chem Soc* **142**, 6400–6408 (2020).

Acknowledgements: We acknowledge the support of this work by the Ontario Research Foundation - Research Excellence Program (number ORF-RE08-034, E.H.S.), the Natural Sciences and Engineering Research Council (NSERC) of Canada number (RGPIN-2017-06477, E.H.S.) and Suncor Canada. I.G. acknowledges the European Union's Horizon 2020 research and innovation programme under Marie Sklodowska-Curie grant (agreement No 846107). DFT calculations were performed on the Niagara supercomputer at the SciNet HPC Consortium. We acknowledge the computational resources supported by SciNet, which is funded by the University of Toronto, the Ontario Research Fund—Research Excellence Program, the Government of Ontario and the Canada Foundation for Innovation. This research used resources of the Advanced Photon Source, an Office of Science User Facility operated for the U.S. Department of Energy (DOE) Office of Science by Argonne National Laboratory and was supported by the U.S. DOE under Contract No. DE-AC02-06CH11357, and the Canadian Light Source and its funding partners. This research used resources of the European Synchrotron Radiation Facility (ESRF) at beamline ID26 during the experimental session MA5352 (DOI 10.15151/ESRF-ES-744180074). The authors thank Dr. Debora Motta Meira from 20BM beamline for their assistance in collecting the XAS data. We thank R. Wolowiec and D. Kopilovic for their kind technical assistance, S. Boccia from the Ontario Centre for the Characterization of Advanced Materials (OCCAM) of the University of Toronto for the electron microscopy imaging and A. Ip. We thank Mr. You-Chiuan Chu and Dr. Hao Ming Chen in the National Taiwan university for conducting in-situ XAS experiments. We thank Dr. Chih-Wen Bao in TPS 44A1, National Synchrotron Radiation Research center, TsinChu, Taiwan for help with tuning the incident beam of XAS. We acknowledge support from the Ministry of Science and Technology, Taiwan (Contracts No. MOST 110-2628-M-002-001-RSP and 110-2113-M-153-001).

Author contributions:

E.H.S. supervised the project. R.D., I.G. and B.-H.L. conceived the idea. R.D., B.-H.L. and I.G. designed and performed the experiments. R.D. with the help of P.F.O. carried out DFT calculations. J.A. performed the XAS experiments. J.A., I.G. and R.D. analyzed the XAS data. A.S.R performed XPS experiments. A.S.R. and I.G. analyzed the XPS data. B.-H.L. and R.D. performed TEM and SEM measruements. R.K.M., E.S., J.W., S.-J.P, G.L and J.-Q.Z. contributed on data interpretation , material synthesis and characterization. R.K.M., C.P.O and D. S. assisted with electrochemical system design. R.D., I.G., B.-H.L., P.F.O. and E.H.S. wrote the manuscript. All authors commented on the manuscript.

Competing interests: The authors declare no competing interests.

Additional Information:

Supplementary information is available in the online version of the paper.

Correspondence and requests for materials should be addressed to E.H.S.